Exploring the 100 au Scale Structure of the Protobinary System NGC 2264 CMM3 with ALMA

Yoshiki Shibayama, Yoshimasa Watanabe, Yoko Oya, Nami Sakai, Ana López-Sepulcre, Sheng-Yuan Liu, Yu-Nung Su, Yichen Zhang, Takeshi Sakai, Tomoya Hirota, et al.

The Astrophysical Journal, 918:32 (16pp), 2021 September 1 https://doi.org/10.3847/1538-4357/ac0ef6

Exploring the 100 au Scale Structure of the Protobinary System NGC 2264 CMM3 with ALMA

Yoshiki Shibayama[1], Yoshimasa Watanabe[2,3], Yoko Oya[1,4], Nami Sakai[3], Ana López-Sepulcre[5,6], Sheng-Yuan Liu[7], Yu-Nung Su[7], Yichen Zhang[3], Takeshi Sakai[8], Tomoya Hirota[9,10], and Satoshi Yamamoto[1,4]
[1] Department of Physics, The University of Tokyo, 7-3-1 Hongo, Bunkyo-ku, Tokyo, 113-0033, Japan
[2] Materials Science and Engineering, College of Engineering, Shibaura Institute of Technology, 3-7-5 Toyosu, Koto-ku, Tokyo 135-8548, Japan; nabe@shibaura-it.ac.jp
[3] Star and Planet Formation Laboratory, RIKEN Cluster for Pioneering Research, Wako, Saitama 351-0198, Japan
[4] Research Center for the Early Universe, The University of Tokyo, 7-3-1, Hongo, Bunkyo-ku, Tokyo 113-0033, Japan
[5] Université Grenoble Alpes, CNRS, IPAG, F-38000 Grenoble, France
[6] IRAM, 300 rue de la piscine, F-38406 Saint-Martin d'Héres, France
[7] Institute of Astronomy and Astrophysics, Academia Sinica, 11F of ASMAB, AS/NTU No.1, Sec. 4, Roosevelt Rd, Taipei 10617, Taiwan
[8] Graduate School of Informatics and Engineering, The University of Electro-Communications, Chofu, Tokyo 182-8585, Japan
[9] National Astronomical Observatory of Japan, Mitaka, Tokyo 181-8588, Japan
[10] Department of Astronomical Sciences, SOKENDAI (The Graduate University for Advanced Studies), Mitaka, Tokyo 181-8588, Japan
Received 2021 March 8; revised 2021 June 25; accepted 2021 June 25; published 2021 September 2

Abstract

We have observed the young protostellar system NGC 2264 CMM3 in the 1.3 mm and 2.0 mm bands at a resolution of about 0.″1 (70 au) with ALMA. The structures of two distinct components, CMM3A and CMM3B, are resolved in the continuum images of both bands. CMM3A has an elliptical structure extending along the direction almost perpendicular to the known outflow, while CMM3B reveals a round shape. We have fitted two 2D Gaussian components to the elliptical structure of CMM3A and CMM3B and have separated the disk and envelope components for each source. The spectral index α between 2.0 and 0.8 mm is derived to be 2.4–2.7 and 2.4–2.6 for CMM3A and CMM3B, respectively, indicating optically thick dust emission and/or grain growth. A velocity gradient in the disk/envelope direction is detected for CMM3A in the CH_3CN, CH_3OH, and $^{13}CH_3OH$ lines detected in the 1.3 mm band, which can be interpreted as the rotation of the disk/envelope system. From this result, the protostellar mass of CMM3A is roughly evaluated to be 0.1–0.5 $M_\odot$ by assuming Keplerian rotation. The mass accretion rate is thus estimated to be $5 \times 10^{-5} - 4 \times 10^{-3}\ M_\odot\ \mathrm{yr}^{-1}$, which is higher than the typical mass accretion rate of low-mass protostars. The OCS emission line shows a velocity gradient in both outflow direction and disk/envelope direction. A hint of outflow rotation is found, and the specific angular momentum of the outflow is estimated to be comparable to that of the disk. These results provide us with novel information on the initial stage of a binary/multiple system.

Unified Astronomy Thesaurus concepts: Star formation (1569); Protostars (1302); Interstellar medium (847); Interstellar molecules (849); Young stellar objects (1834)

1. Introduction

It is well known that a significant fraction of stars are born in binary or multiple systems (e.g., Duchêne & Kraus 2013): the fraction is about one-half for solar-type stars (Raghavan et al. 2010). Hence, formation of binary systems is a central issue for the study of star formation. Thanks to the development of radio interferometry, more and more protostellar sources are now found to be binary or multiple systems. For instance, survey observations of protostars in Perseus and Orion have been intensively conducted with the Atacama Large Millimeter/submillimeter Array (ALMA) and the Very Large Array (e.g., Tobin et al. 2016, 2018, 2020; Maury et al. 2019) and many binary and multiple protostellar systems have been identified in these observations. For instance, the multiplicity fraction is reported to be 0.57 ± 0.09 for Class 0 protostars in Perseus (Tobin et al. 2016). Maury et al. (2019) reported a multiplicity fraction of $<0.57 \pm 0.10$ based on the observation of 16 Class 0 protostars in various regions. Studies on gas kinematics of binary systems have also been conducted by observing molecular emission lines (e.g., Tobin et al. 2019; Maureira et al. 2020; Oya & Yamamoto 2020; Takakuwa et al. 2020). To elucidate the formation process of a binary or multiple system, it is still of fundamental importance to reveal its early phase for several prototypical objects under various environmental conditions. To start with, we here report the case of the very young protostellar source in the high-mass star-forming region NGC 2264.

NGC 2264 is an active star-forming region near the Solar system (719 ± 16 pc: Maíz Apellániz 2019). It belongs to the Monoceros OB1 association consisting of hundreds of near-infrared sources (Lada & Lada 2003). The brightest infrared source is IRS1 (Allen 1972) whose mass is reported to be ~9.5 $M_\odot$ (Thompson et al. 1998). Around IRS1, 12 dense cores, called CMM1—CMM12, are distributed within a 4′ (1 pc) area, among which CMM3 is the most massive core (40 $M_\odot$: Peretto et al. 2006). Ward-Thompson et al. (2000) suggested that CMM3 will form a single high-mass star, or a few intermediate-mass stars. Maury et al. (2009) reported that CMM3 will form a single protostar that will evolve into a main-sequence star with a mass of 8 $M_\odot$ by using the theoretical evolutionary track. Saruwatari et al. (2011) detected

Table 1
Emission Lines Analyzed in This Study

Emission Line	Rest. Freq.[a] (GHz)	E_l[a,b] (cm^{-1})	$S\mu^2$ [a] (Debye^2)	Beam Size	σ[c] (Jy beam^{-1})
Continuum (1.3 mm)	241			$0\farcs104 \times 0\farcs073$ (P.A. $= -42\fdg9$)	1.3×10^{-4}
Continuum (2.0 mm)	155			$0\farcs069 \times 0\farcs060$ (P.A. $= -38\fdg7$)	3.8×10^{-5}
CH_3CN ($14_4 - 13_4$)	257.4481282	135.2681	395.5	$0\farcs112 \times 0\farcs100$ (P.A. $= -55\fdg0$)	3.8×10^{-3}
CH_3CN ($14_3 - 13_3$)	257.4827919	100.5247	410.93	$0\farcs112 \times 0\farcs100$ (P.A. $= -55\fdg0$)	3.8×10^{-3}
OCS (20 − 19)	243.2180364	77.0793	10.23	$0\farcs119 \times 0\farcs106$ (P.A. $= -53\fdg9$)	3.1×10^{-3}
CH_3OH ($16_{3,14} - 16_{2,15}$ A)	255.2418880	245.4316	59.41	$0\farcs114 \times 0\farcs103$ (P.A. $= -59\fdg2$)	3.5×10^{-3}
$^{13}CH_3OH$ ($4_{3,2} - 4_{2,3}$ A)	255.2037280	42.018	2.9516	$0\farcs114 \times 0\farcs103$ (P.A. $= -59\fdg2$)	3.5×10^{-3}
$^{13}CH_3OH$ ($8_{3,6} - 8_{2,7}$ A)	255.2656370	82.948	7.2912	$0\farcs114 \times 0\farcs103$ (P.A. $= -59\fdg2$)	3.5×10^{-3}

Notes.—For the continuum emission, the center frequency of the spectral window is given.
[a] Taken from CDMS (Endres et al. 2016).
[b] Lower-state energy.
[c] rms noise level.

an outflow associated with CMM3 whose dynamical timescale is as short as 140–2000 yr. Since CMM3 is deeply embedded in the parent core, it is thought to be in an early stage of high-mass star formation. However, a high spatial resolution observation with ALMA revealed that this picture forming a single high-mass star is too simplified. Watanabe et al. (2017) conducted subarcsecond resolution observations ($\sim 0\farcs3$) with ALMA and found that this object is a complex system mainly consisting of CMM3A and CMM3B. Furthermore, they are surrounded by several faint continuum sources (CMM3C-H). Therefore, CMM3 is now recognized as a good target with which we can study the early phase of the intermediate-mass binary formation in a cluster-forming environment.

Watanabe et al. (2017) presented another interesting feature of this source, a significant difference of the spectral appearance between CMM3A and CMM3B. Very rich molecular lines of complex organic molecules such as CH_3OH, $HCOOCH_3$, and $(CH_3)_2O$ are detected in CMM3A, indicating a hot core/hot corino associated with CMM3A. On the other hand, a very sparse spectrum is observed for CMM3B. Watanabe et al. (2017) proposed the following possibilities of the origin of such a striking difference: (1) a chemical difference due to different evolutionary stages of the two protostars, (2) the effect of the dust opacity, and (3) the difference in the masses of the two protostars. A similar case showing a different spectral appearance between the binary components was reported for NGC 1333 IRAS4A (López-Sepulcre et al. 2017). For this source, it has been reported that the dust opacity causes the difference (Sahu et al. 2019; De Simone et al. 2020). To investigate the NGC 2264 CMM3 case, observations of the dust emission at multiple frequencies are thus needed.

As described above, NGC 2264 CMM3 is an interesting testbed for exploring the physics and chemistry of binary formation in a cluster-formation environment. To evaluate the protostellar mass and characterization of the disk/envelope structure for each component, we have observed the CMM3 region with ALMA at an angular resolution of about $0\farcs1$, which is three times higher than that of the preceding study. We have analyzed the distribution of the dust-continuum emission at 1.3 and 2.0 mm to extract the disk component. We have also investigated the kinematics of CMM3A by using molecular lines to evaluate its protostellar mass. This observation will provide us with a clue to discriminating the above possibilities for the different spectral appearance between the two components raised by Watanabe et al. (2017).

2. Observation and Data Reduction

The observation in Band 6 (1.3 mm) was carried out on 2019 August 9 with 39 antennas. The baseline length on the ground ranged from 43.3 to 5893.6 m. Six spectral windows with a bandwidth of 117 MHz each and a frequency resolution of 0.12 MHz (velocity resolution of 0.14 km s^{-1} at 255 GHz) were employed for molecular line observations, while one spectral window with a bandwidth of 1.875 GHz and a frequency resolution of 0.98 MHz (velocity resolution of 1.2 km s^{-1} at 255 GHz) was mainly used for the continuum observation. The field center is $(\alpha_{\rm ICRS}, \delta_{\rm ICRS}) = (06^{\rm h}41^{\rm m}12\fs2800, 09\arcdeg29\arcmin12\farcs000)$. The total on-source time was 31.62 minutes. The largest recoverable angular scale is $1\farcs3$ (930 au). J0725 −0054 was used for the bandpass calibration and the flux calibration, while J0643+0857 was used for the phase calibration. The molecular lines used in this study are listed in Table 1.

The continuum observation in Band 4 (2.0 mm) was carried out on 2019 July 16 with 46 antennas. The baseline length on the ground ranged from 92.1 to 8547.6 m. Four spectral windows with a bandwidth of 938 MHz and a frequency resolution of 0.49 MHz (0.95 km s^{-1} at 155 GHz) were employed. The field center is the same as that in the Band 6 observation. The total on-source time was 38.42 minutes. The largest recoverable angular scale was $1\farcs2$ (860 au). J0725 −0054 was used for the bandpass calibration and the flux calibration, while J0643+0857 was used for the phase calibration.

Data reduction was carried out with the Common Astronomy Software Applications package (CASA).[11] Self-calibration was performed for phase and amplitude by using the continuum data and was applied to the line data. Continuum images were obtained by averaging line-free channels, where the Briggs' weighting with a robustness parameter of 0.0 is employed for the CLEAN process. Six data cubes for the molecular lines listed in Table 1 were obtained after subtracting the continuum component from the visibility data and were CLEANed with automasking and Briggs weighting with a robustness parameter of 0.5. The synthesized beam sizes are summarized in Table 1.

[11] https://casa.nrao.edu/

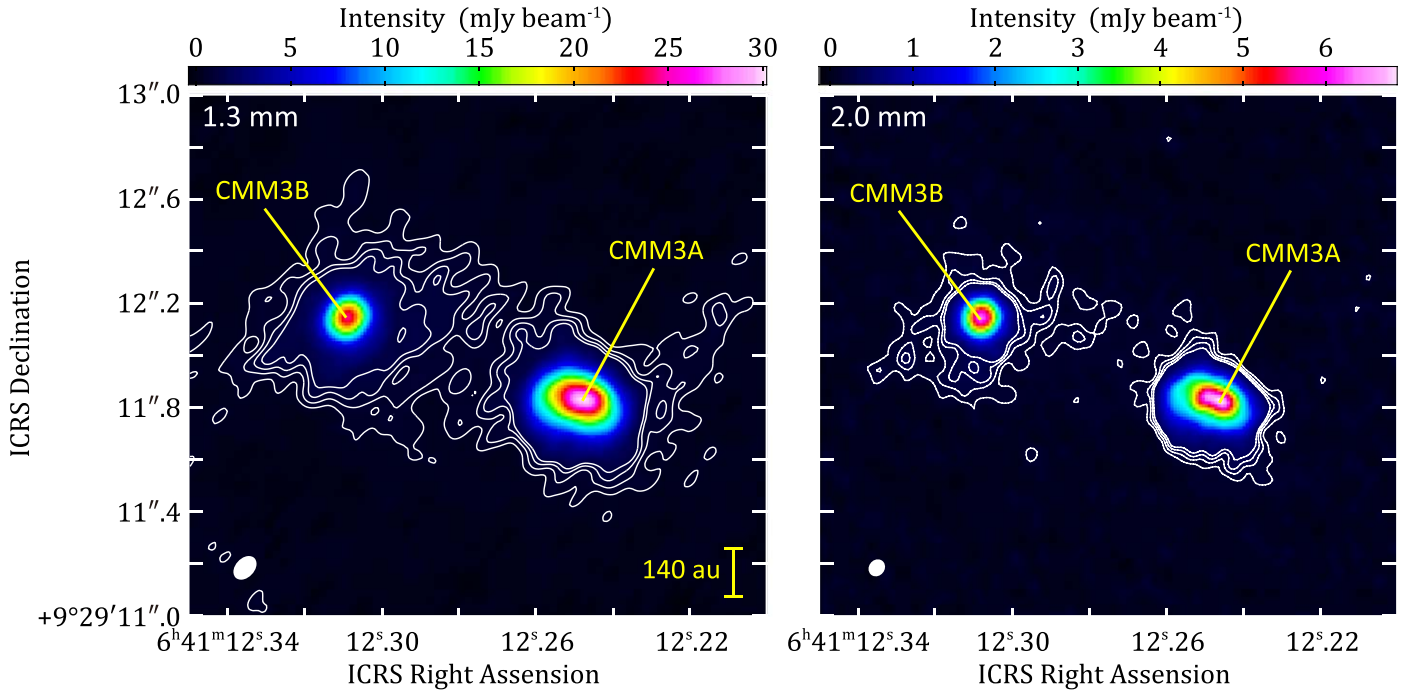

Figure 1. The 1.3 mm (Band 6) and 2.0 mm (Band 4) continuum images of CMM3A and CMM3B (Band 6 and Band 4). The white ellipse at the lower left corner of each image represents the beam size. Contours levels are $\sigma \times$ (3, 5, 7, 9). $\sigma = 0.13$ mJy beam^{-1} for 1.3 mm and 3.8×10^{-2} mJy beam^{-1} for 2.0 mm.

Velocity resolutions of all the cubes were set to 0.25 km s^{-1}. The rms noises of the images are shown in Table 1. We estimate an uncertainty of the absolute flux scale to be 10%[12] in the observations with Band 4 and Band 6.

3. Results and Discussion

3.1. Continuum Images

Figure 1 shows the 1.3 mm (Band 6) and 2.0 mm (Band 4) continuum images. Two dust-continuum peaks, CMM3A and CMM3B, are clearly seen. The two sources are well separated by 0.″95 (680 au), although they look loosely connected with each other by a weak parental envelope, as seen in the 1.3 mm image.

The total fluxes at 1.3 mm of CMM3A and CMM3B over the $0.''6 \times 0.''6$ area are 191 ± 19 mJy and 99 ± 10 mJy, respectively. The sum of these two fluxes is smaller than the total 1.3 mm flux of CMM3 (472 mJy) observed with the $3.''18 \times 2.''67$ beam of SMA even if we take into account of the flux uncertainty of 20% in the observation with SMA (Saruwatari et al. 2011). Furthermore, it is much smaller than the 1.2 mm flux (1108 mJy) and 1.3 mm flux (1500 mJy) observed by Peretto et al. (2006) and Ward-Thompson et al. (2000), respectively, using single-dish telescopes. Contrary to these previous studies, we are just looking at much smaller structures with the largest recoverable scale of 1.″3. Hence, the extended component of CMM3 is heavily resolved-out in this observation.

Assuming that the dust-continuum emission is optically thin, the total gas mass of CMM3A and CMM3B are evaluated to be 0.11–0.24 $M_\odot$ and 0.05–0.11 $M_\odot$, respectively, from the 1.3 mm data by using the following equation:

$$M_g = \frac{S_\nu d^2}{\kappa_\nu B_\nu(T_d) R_d}, \quad (1)$$

where M_g is the total gas mass, S_ν is the total flux, d is the distance to NGC 2264 (719 ± 16 pc: Maíz Apellániz 2019), κ_ν is the frequency-dependent dust-mass opacity coefficient, $B_\nu(T_d)$ is the blackbody function of Planck's law at the dust temperature T_d, and R_d is the dust-to-gas mass ratio. κ_ν and R_d are assumed to be 1.3 cm^2 g^{-1} at 1.3 mm and 0.01 mm, respectively, as adopted by López-Sepulcre et al. (2017). The κ_ν value is originally given in Ossenkopf & Henning (1994). T_d is assumed to be in the range 100–200 K. If the dust-continuum emission is optically thick, the total gas mass derived above is regarded as the lower limit.

CMM3A has an elliptical structure extending in the east–west direction. To define its distribution, we first try to fit a single 2D Gaussian function to the 2.0 mm continuum image, where the effect of the synthesized beam is taken into account. However, we find that a fairly large residual is left in the image after subtracting the single 2D Gaussian model, as shown in 2(f). A similar residual is seen in the single 2D Gaussian fit to the 1.3 mm continuum image (see the Appendix). The residuals seem to originate from the excess emission in the southern part. Then, we conduct a double 2D Gaussian fitting on the image plane, which means the fitting with two 2D Gaussian components. Figures 2(b)–(e) show the result. The systematic residuals in the single 2D Gaussian fitting are almost eliminated, as shown in Figure 2(e) (also see the Appendix for the 1.3 mm data). The fitted Gaussian components are shown in Figures 2(c), (d) for the 2.0 mm image, while those for the 1.3 mm image are in the Appendix. The fitting parameters are summarized in Table 2. CMM3A consists of compact and extended components. The compact component

[12] ALMA Cycle 7 Technical Handbook (https://almascience.nrao.edu/documents-and-tools/cycle7/alma-technical-handbook/).

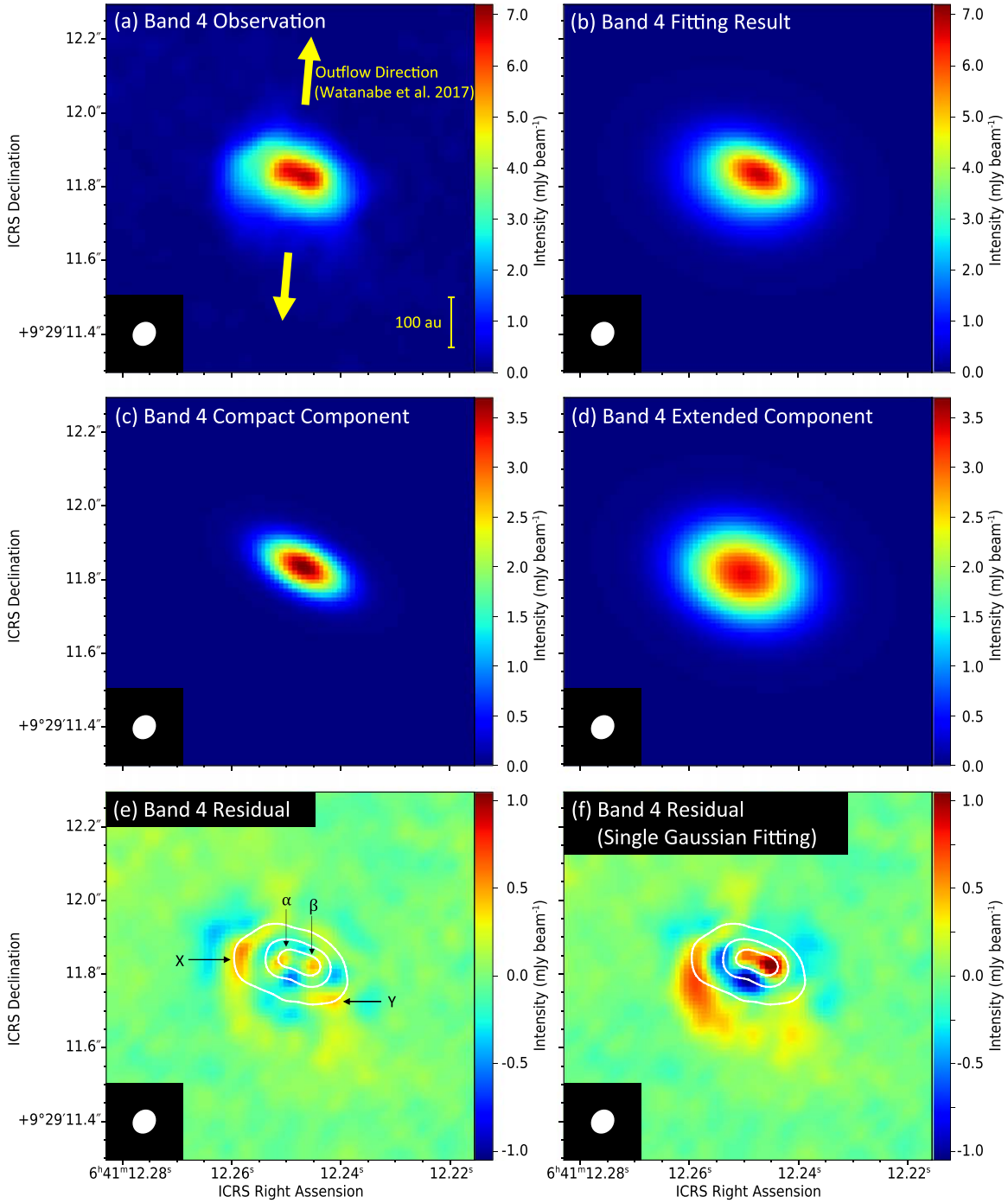

Figure 2. (a) The 2.0 mm (Band 4) continuum image of CMM3A. (b) The result of a double 2D Gaussian fit. (c), (d) The compact and extended components of the fitted double 2D Gaussian convolved with the beam. (e) Residuals of the double 2D Gaussian fitting. (f) Residuals of the single 2D Gaussian fitting for comparison. The continuum emission at 2.0 mm is displayed in contours with steps of 50σ where σ is 3.8×10^{-2} mJy beam^{-1} in (e) and (f). X and Y denote the position of the systematic residuals also seen in the residuals of the double 2D Gaussian fit for the 1.3 mm continuum (see the Appendix). For α and β, see Section 3.1.

can be interpreted as the disk structure, while the extended component is the surrounding envelope structure. Both components extend in a direction almost perpendicular to the outflow of CMM3A, which blows along the P.A. of $-5°$ (Saruwatari et al. 2011; Watanabe et al. 2017).

Assuming that the compact component is an inclined thin disk, the inclination angle i with respect to the line of sight (i.e., $i = 90°$ for the edge-on case) is evaluated to be 65° from the deconvolved sizes of the major and minor axes. This inclination angle is regarded as the lower limit because the thickness of the disk is ignored. If the thickness is considered, the inclination angle can be larger to reproduce the sizes of the major and minor axes. Thus, the inclination of the disk of CMM3A likely has a nearly edge-on configuration. This result is consistent with the previous observation of the outflow by Saruwatari et al. (2011). We then evaluate the thickness of the inner envelope. Assuming that the extended component is an inclined thick disk with the same inclination angle as that of the compact component, the thickness h is evaluated to be 70–90 au. This value is about a third of the size of the major

Table 2
The Fitting Parameters of the Double 2D Gaussian Fitting[a]

Band	Source	Component	Major Axis[b] (FWHM)	Minor Axis[b] (FWHM)	P.A.[b]	R.A. (ICRS)	Decl. (ICRS)	Peak Intensity
Band 4	CMM3A	Compact	$0\farcs164 \pm 0\farcs001$ (118 ± 3 au)	$0\farcs059 \pm 0\farcs001$ (42.3 ± 0.9 au)	$62\fdg8 \pm 0\fdg3$	$06^{h}41^{m}12\fs246$	$09°29'11\farcs835$	3.79 mJy beam^{-1}
		Extended	$0\farcs275 \pm 0\farcs001$ (198 ± 4 au)	$0\farcs1915 \pm 0\farcs0009$ (138 ± 3 au)	$76\fdg5 \pm 0\fdg4$	$06^{h}41^{m}12\fs250$	$09°29'11\farcs818$	3.38 mJy beam^{-1}
	CMM3B	Compact	$0\farcs0997 \pm 0\farcs0003$ (72 ± 2 au)	$0\farcs0979 \pm 0\farcs0003$ (70 ± 2 au)	$87° \pm 6°$	$06^{h}41^{m}12\fs308$	$09°29'12\farcs146$	6.04 mJy beam^{-1}
		Extended	$0\farcs547 \pm 0\farcs006$ (393 ± 9 au)	$0\farcs382 \pm 0\farcs004$ (276 ± 6 au)	$105\fdg7 \pm 0\fdg7$	$06^{h}41^{m}12\fs308$	$09°29'12\farcs080$	0.37 mJy beam^{-1}
Band 6	CMM3A	Compact	$0\farcs190 \pm 0\farcs002$ (137 ± 3 au)	$0\farcs067 \pm 0\farcs002$ (48 ± 1 au)	$62\fdg3 \pm 0\fdg3$	$06^{h}41^{m}12\fs247$	$09°29'11\farcs837$	14.6 mJy beam^{-1}
		Extended	$0\farcs266 \pm 0\farcs001$ (191 ± 4 au)	$0\farcs192 \pm 0\farcs001$ (138 ± 3 au)	$68\fdg8 \pm 0\fdg4$	$06^{h}41^{m}12\fs250$	$09°29'11\farcs815$	17.2 mJy beam^{-1}
	CMM3B	Compact	$0\farcs1072 \pm 0\farcs0003$ (77 ± 2 au)	$0\farcs0994 \pm 0\farcs0004$ (71 ± 2 au)	$60\fdg7 \pm 1\fdg4$	$06^{h}41^{m}12\fs309$	$09°29'12\farcs145$	22.4 mJy beam^{-1}
		Extended	$0\farcs538 \pm 0\farcs005$ (386 ± 9 au)	$0\farcs393 \pm 0\farcs004$ (283 ± 6 au)	$104\fdg4 \pm 0\fdg7$	$06^{h}41^{m}12\fs306$	$09°29'12\farcs100$	2.1 mJy beam^{-1}

Notes.—Errors are standard deviations except for the sizes of major and minor axes in au whose errors are mainly determined by the uncertainty of the distance to NGC 2264 (719 ± 16 pc: Maíz Apellániz 2019).
[a] The fitting is done on the image plane.
[b] Beam-deconvolved size.

axis (200 au), and hence, the inner envelope seems to have a flattened structure.

After subtracting the fitted double 2D Gaussian functions from the observed images, a faint residual pattern still remains in the eastern (X) and southwestern (Y) sides of CMM3A in both 2.0 and 1.3 mm data, the former of which is shown in Figure 2(e) (see the Appendix for the 1.3 mm data). These patterns may represent internal structures of CMM3A. In addition, the two peaks of the residual (α and β) can be seen in the compact component in the 2.0 mm data (Figure 2(e)), which is symmetrically located with respect to the peak of the compact Gaussian component. This means that the compact component has a flat-topped or double-peaked structure. Such a structure is not seen in Band 6 probably because of the lower angular resolution and/or higher dust opacity. This structure may be caused by a saturation effect due to high opacity. Alternatively, it may represent a substructure within the compact component or a possibility of a close binary system with a separation of about 70 au.

The structure of CMM3B was also fitted better with double 2D Gaussian functions than with a single 2D Gaussian function (see Figure 3 for the 2.0 mm data and the Appendix for the 1.3 mm data). The fitting parameters are summarized in Table 2. The distribution is composed of the compact and extended components. In contrast to the CMM3A case, the compact component has a nearly round shape.

3.2. Continuum Spectrum

In this subsection, we investigate the spectral energy distribution (SED) by using the 1.3 and 2.0 mm continuum images in combination with the 0.8 mm (350 GHz) image previously observed with ALMA (Watanabe et al. 2017). We use the total fluxes over a $0\farcs6 \times 0\farcs6$ area for CMM3A and CMM3B to cover their extended structures. The two areas for the flux measurement do not overlap with each other because the separation between CMM3A and CMM3B is $0\farcs95$. The disk and envelope structures of CMM3A are not distinguished here.

Figure 4 shows the SED plots for CMM3A and CMM3B. The power-law index (α) of the spectral energy distribution ($I(\nu) \propto \nu^{\alpha}$) derived from total fluxes is 2.4–2.7 for CMM3A and 2.4–2.6 for CMM3B. These values are rather small and close to the Rayleigh–Jeans limit ($\alpha = 2$). In interstellar clouds, the α index is mostly in a range of 3.5–4.0 (Li & Draine 2001). It decreases as dust drains grow in protoplanetary disks (e.g., Pérez et al. 2015). Grain growth has recently been reported for disk structures in the low-mass Class 0 and Class I sources (e.g., Gerin et al. 2017; Friesen et al. 2018). Thus, grain growth could be a possible cause of the small α indices. Alternatively, the α index can be close to 2 if the dust-continuum emission is optically thick. An effect of the dust scattering may also contribute to the small index (Liu 2019). Indeed, the peak brightness temperature of the continuum emission at 1.3 mm is 76–92 K and 62–76 K for CMM3A and CMM3B, respectively. Considering that CMM3A and CMM3B are expected to be young ($\sim$1000 yr) protostars, we think that the observed spectral indices imply high dust opacities for CMM3A and CMM3B. We will come back to this point along with the results of molecular line observations (Section 3.3).

For further investigation, we evaluate the spectral indices of the compact and extended components by using the 1.3 mm and 2.0 mm total fluxes over a $0\farcs6 \times 0\farcs6$ area. Table 3 shows the result, where the fluxes are derived by integrating those of a 2D Gaussian model within the area. The spectral indices of both components are 2.2–3.2 for CMM3A. For CMM3B, the spectral index of the compact and extended components are 1.9–2.8 and 2.6–3.5, respectively. Despite large uncertainties, the results are almost consistent with those derived for the whole structures of CMM3A and CMM3B by using the three bands. In addition, we also derive the spectral indices for CMM3A and CMM3B by using the fluxes measured with the $0\farcs381 \times 0\farcs308$ area (Table 3). The spectral indices thus obtained are slightly smaller than those derived for the

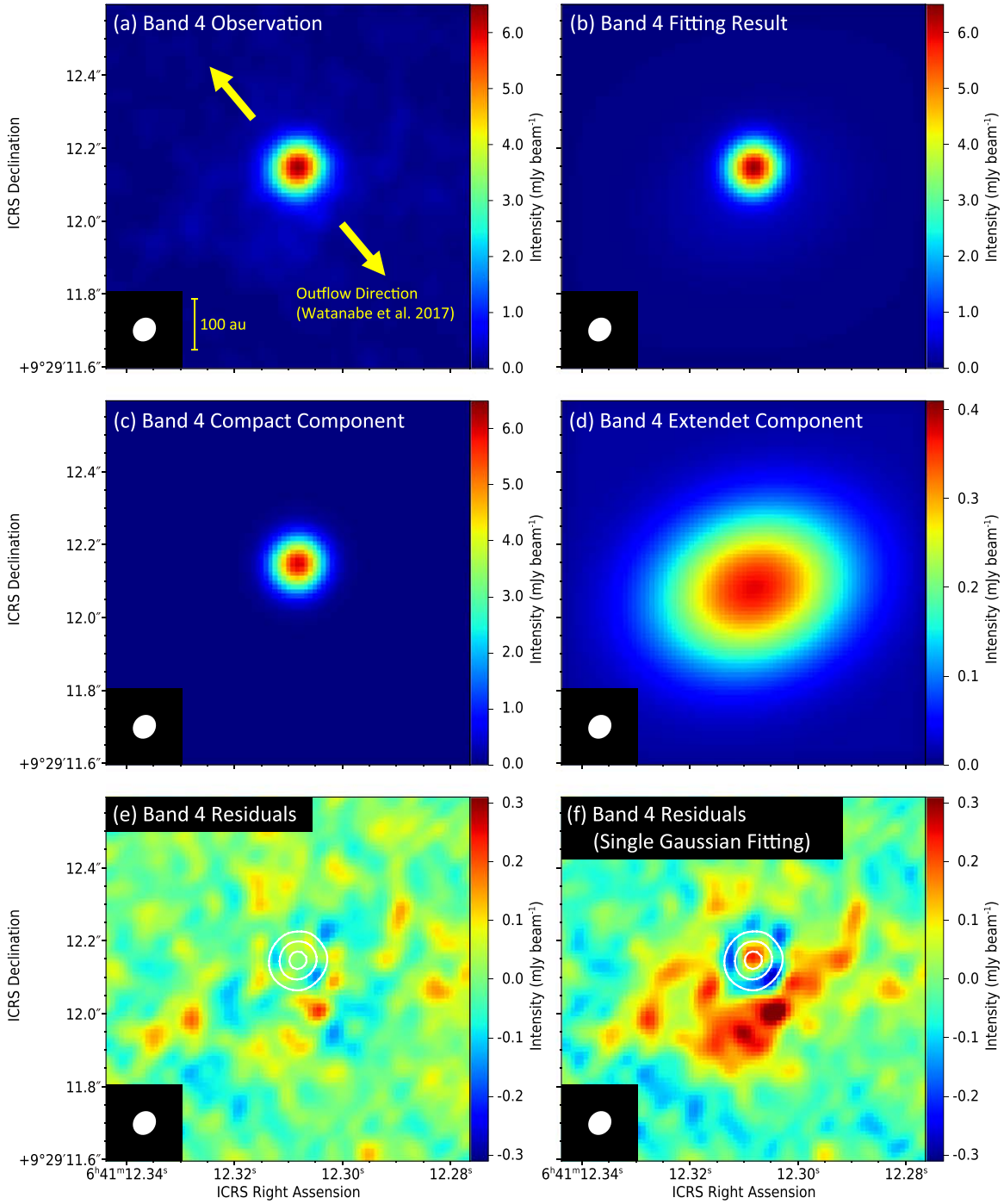

Figure 3. (a) The 2.0 mm (Band 4) continuum image of CMM3B. (b) The result of a double 2D Gaussian fit. (c), (d) The compact and extended components of the fitted double 2D Gaussian convolved with the beam. Note that the color scale is different between (c) and (d). (e) Residuals of the double 2D Gaussian fitting. (f) Residuals of the single 2D Gaussian fitting for comparison. The continuum emission at 2.0 mm is displayed in contours with steps of 50σ where σ is 3.8×10^{-2} mJy beam^{-1} in (e) and (f).

$0\farcs6 \times 0\farcs6$ area because of the smaller contribution of the extended part of the envelope having a larger index.

3.3. Molecular Distribution

Figure 5 shows the spectra observed at the continuum peaks of CMM3A and CMM3B in the 1.3 mm band. The spectra are prepared by using (a part of) the spectral window for the continuum observation with the synthesized beam. Here, we employ the systemic velocities of 7.4 km s^{-1} and 7.8 km s^{-1} for CMM3A and CMM3B, respectively (Watanabe et al. 2017). The spectrum of CH_3OH observed at room temperature in a laboratory is also shown for reference (Watanabe et al. 2021). Molecular emission lines in this figure mostly come from the torsionally excited CH_3OH (v_t= 1). The spectrum is rich in CMM3A but sparse in CMM3B, as found in the 0.8 mm band by Watanabe et al. (2017). Because of the congested spectrum of CMM3A, molecular lines are often contaminated by other molecular lines. To investigate the kinematic structure, we select six uncontaminated molecular lines among the lines

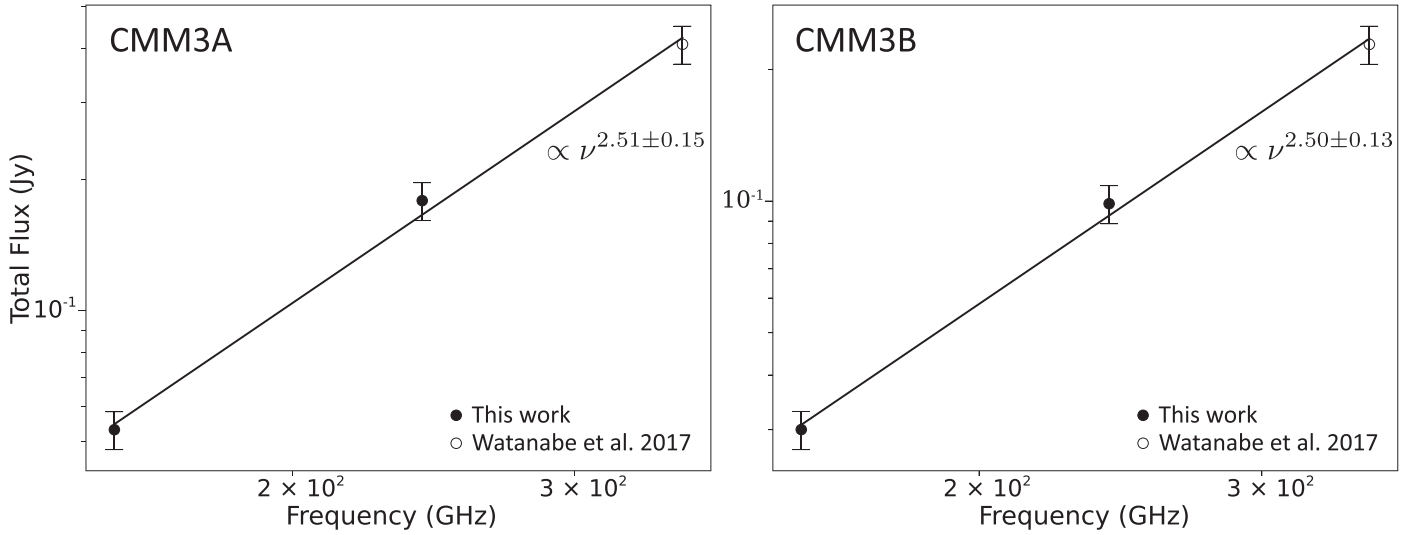

Figure 4. The spectral index derived from the total flux. The closed circles represent the results of this work, while the open circle represents the 0.8 mm data taken from Watanabe et al. (2017). The horizontal axis shows the frequency of the continuum images and the longitudinal axis shows the total flux. Errors are 10% of each total flux. The flux is measured for a $0\farcs6 \times 0\farcs6$ area for CMM3A and CMM3B.

Table 3
Spectral Indices

Source	Component	Spectral Index[a]	Area[b]	Used Bands (mm)
CMM3A	Total	2.4–2.7	$0\farcs6 \times 0\farcs6$	2.0, 1.3, 0.8
	Compact	2.2–3.1	$0\farcs6 \times 0\farcs6$	2.0, 1.3
	Extended	2.3–3.2	$0\farcs6 \times 0\farcs6$	2.0, 1.3
	Peak	2.2–2.5	$0\farcs38 \times 0\farcs31$, P.A. $= -35\fdg4$	2.0, 1.3, 0.8
CMM3B	Total	2.4–2.6	$0\farcs6 \times 0\farcs6$	2.0, 1.3, 0.8
	Compact	1.9–2.8	$0\farcs6 \times 0\farcs6$	2.0, 1.3
	Extended	2.6–3.5	$0\farcs6 \times 0\farcs6$	2.0, 1.3
	Peak	1.9–2.4	$0\farcs38 \times 0\farcs31$, P.A. $= -35\fdg4$	2.0, 1.3, 0.8

Notes.
[a] Ranges are derived from the estimated errors of the flux (10%).
[b] The area in which the flux is evaluated.

observed at a high frequency resolution as listed in Table 1. Here, line contamination is checked by using the spectral line databases: The Cologne Database for Molecular Spectroscopy (CDMS: Endres et al. 2016) and the Jet Propulsion Laboratory (JPL) catalog (Pickett et al. 1998). Figure 6 shows the spectral profiles of the selected lines observed at CMM3A.

Figure 7 shows the zeroth moment maps (integrated intensity maps) of the six selected lines in the 1.3 mm band. Figure 8 depicts the zeroth moment maps expanded around CMM3A and the corresponding first moment maps. As shown in Figure 7, emission lines are detected in CMM3A, while no lines except for the faint OCS ($J = 20 - 19$) line are detected in CMM3B with the rms sensitivity of 5 mJy beam^{-1} km s^{-1}. These emission lines detected in CMM3A show a velocity gradient along the east–west direction (redshifted in the eastern side and blueshifted in the western side), as revealed in the first moment maps in Figure 8. For CH_3OH and $^{13}CH_3OH$, the velocity gradient is almost along the elongated shape of the continuum images, and hence, the velocity gradients are most likely interpreted as the rotation motion of CMM3A. On the other hand, the gradient for CH_3CN and OCS seems to be a combination of the outflow and the rotation of the disk/envelope system, considering that the outflow of CMM3A blows along the P.A. of $-5°$ (Saruwatari et al. 2011; Watanabe et al. 2017).

It should be noted that the zeroth moment maps of CH_3CN ($14_4 - 13_4$ and $14_3 - 13_3$), OCS ($20 - 19$), and CH_3OH ($16_{3,14} - 16_{2,15}$ A) show the distributions extending to the north and south directions from the protostar with slight depression along the midplane of the disk/envelope structure where the continuum emission is bright. In contrast, the zeroth moment maps of $^{13}CH_3OH$ do not clearly show such features. Hence, the depression along the disk midplane seems to originate from the high opacity of dust-continuum and molecular line emissions. The observed intensity is approximately proportional to $\{1 - \exp(-\tau_\nu)\}$, where τ_ν is approximately the sum of the optical depth of the molecular lines and that of the dust. In the optically thin case ($\tau_\nu \ll 1$), the intensity is proportional to the optical depth, and the observed intensity is the sum of the intensity of the emission line and that of the continuum image. After subtracting the continuum emission, just a line image is observed. However, in the optically thick case, the observed intensity is saturated at a fixed value and not proportional to the optical depth. Thus, the observed intensity is not the sum of the intensity of the emission line and that of the continuum image. Since we obtain data cubes for molecular lines by subtracting the intensity of the continuum image from the observed intensity, the line intensity becomes lower in this case for the region where the intensity of the continuum is high. This situation is actually

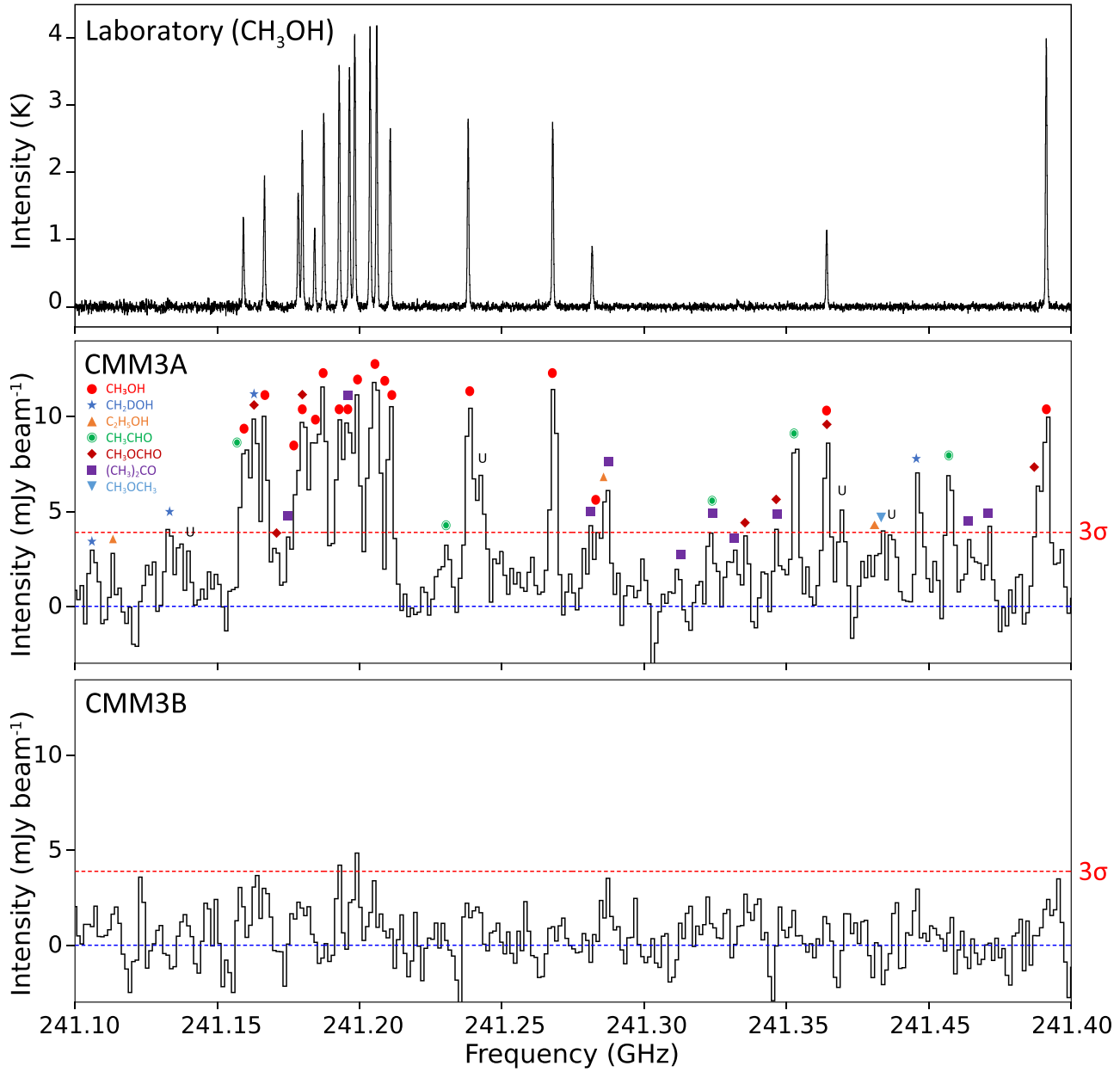

Figure 5. (Middle and Bottom) Spectra observed at the continuum peaks of CMM3A and CMM3B. The red line represents the 3σ level ($\sigma = 2.0$ K). The frequency resolution is 0.98 MHz. (Top) CH_3OH lines observed at room temperature in a laboratory (Watanabe et al. 2021). Molecular lines are rich in CMM3A and deficient in CMM3B as found by Watanabe et al. (2017).

reported in HH212, which is known as a "hamburger"-shaped dusty disk: the intensities of the molecular emissions show depression in the midplane of the disk (Codella et al. 2018; Lee et al. 2018).

Judging from the spectral index derived from the continuum images, the dust opacity of CMM3A would be high in the disk region. On the basis of the outflow morphology (Saruwatari et al. 2011), the disk of CMM3A is nearly edge-on (inclination angle $\sim 60^\circ$). Therefore, the dust opacity could be particularly high around the midplane of the disk. This seems to contribute to the depression of the intensity along the disk structure. The emission lines of CH_3CN, OCS, and CH_3OH are expected to be optically thick around the midplane of the disk/envelope structure, while those of $^{13}CH_3OH$ are not. In Figure 5, the CH_3OH emission lines in CMM3A indeed look almost saturated to a certain level of intensity, although the laboratory spectrum shows intensity variation from line to line. The $CH_3OH(16_{3,14} - 16_{2,15}\,A)$ line should be optically thick, as the $^{13}CH_3OH(8_{3,6} - 8_{2,7}\,A)$ line is observed with the comparable intensity. The optical depth of the CH_3OH line is roughly estimated to be 50 or larger, assuming an LTE condition with a temperature higher than 100 K. Moreover, the CH_3CN $14_3 - 13_3$ emission is expected to be brighter by a factor of 2 or more than the $14_4 - 13_4$ emission, because the nuclear spin degeneracy of the former emission is twice as large as that of the latter emission. Nevertheless, these emission lines have similar intensities in Figure 6, which indicates the high optical depths of these lines. A similar case for the CH_3CN lines is often reported in high-mass star-forming regions (e.g., Furuya et al. 2011; Ilee et al. 2018). Thus, the line optical depth would also contribute to the intensity depression.

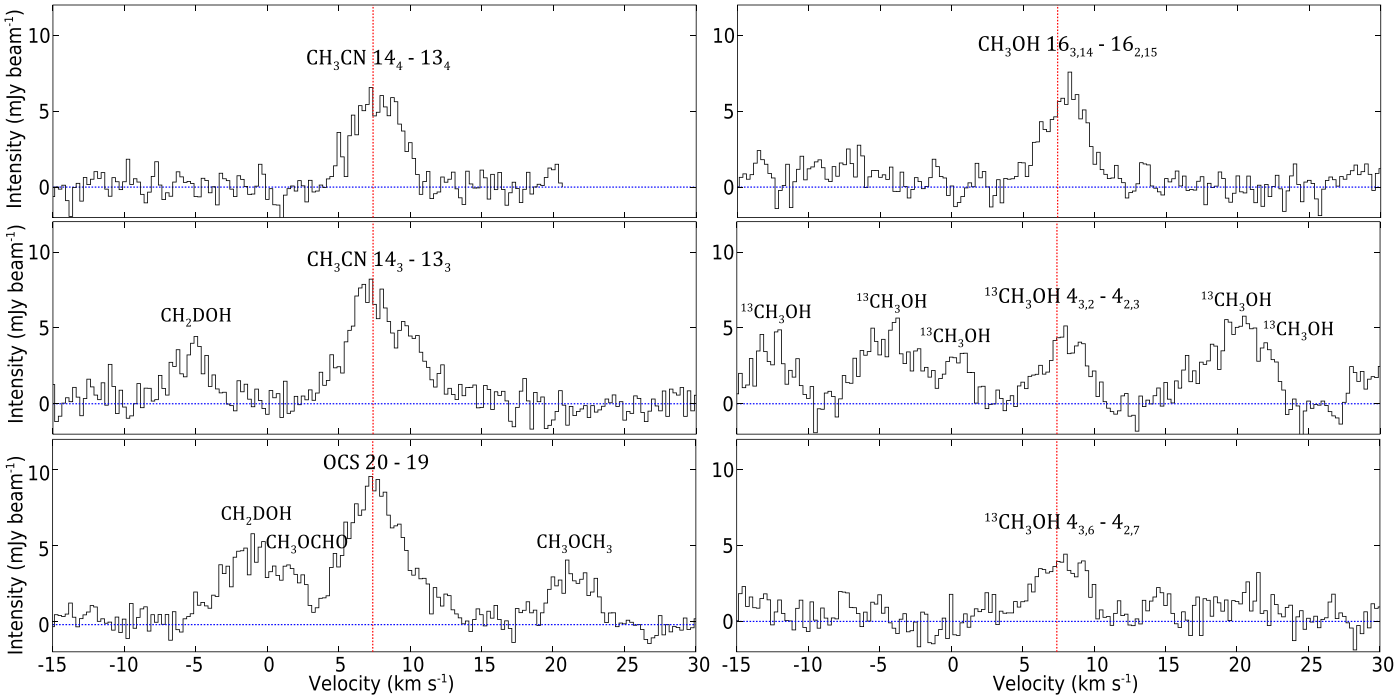

Figure 6. Spectral profiles of the molecular lines listed in Table 1, which are observed toward CMM3A. The spectra are prepared by averaging the $0\farcs6 \times 0\farcs6$ area. The velocity resolution is 0.25 km s^{-1}. The vertical red line represents the systemic velocity of CMM3A (7.4 km s^{-1}: Watanabe et al. 2017).

Likewise, the very sparse spectral lines toward CMM3B could be interpreted as the effect of the high dust optical depth, as in the case of NGC 1333 IRAS 4A1 (De Simone et al. 2020). Centimeter wave observations of the continuum and line emissions are essential to confirm this interpretation.

3.4. Rotation of the CMM3A Disk

We find a rotation motion of the disk for CMM3A in the CH_3CN, OCS, CH_3OH, and $^{13}CH_3OH$ lines (Section 3.3). To analyze their velocity structures in detail, we prepare the position–velocity (PV) diagrams of CH_3CN, OCS, and CH_3OH along the disk/envelope direction (Figure 9). Although the PV diagrams are patchy due to a poor signal-to-noise ratio, the velocity gradient along the disk/envelope direction is indeed detected for these lines. It is, however, difficult to distinguish between the Keplerian rotation and the infalling rotating motion conserving the angular momentum (cf. Oya et al. 2016, 2018). Then, we roughly estimate the protostellar mass of CMM3A, assuming the Keplerian rotation as:

$$|v| = \sqrt{\frac{GM_{\rm ps}}{r}}\,\sin i. \qquad (2)$$

Here, v is the velocity along the line of the sight, G is the gravitational constant, $M_{\rm ps}$ is the mass of the protostar, r is the distance from the protostar, and i is the inclination angle of the disk. The Keplerian velocities for the masses of 0.1, 0.5, and 1 $M_\odot$ are plotted on Figure 9, where the inclination angle of the disk is assumed to be 65°. It is difficult to determine the mass precisely because of a poor S/N ratio of the PV diagram. Nevertheless, the mass of the protostar is roughly constrained to be 0.1–0.5 $M_\odot$ by comparing the rotation curves with the observed PV diagrams. Since the protostar is deeply embedded in a massive and accreting parent core (Maury et al. 2009), the relatively low protostellar mass means the infancy of the protostar.

Saruwatari et al. (2011) found the dynamical timescale of the outflow of CMM3A is 140–2000 yr. Dividing the estimated protostellar mass of 0.1–0.5 $M_\odot$ by the dynamical timescale, the average mass accretion rate of CMM3A is estimated to be $5 \times 10^{-5} - 4 \times 10^{-3}\ M_\odot\ {\rm yr}^{-1}$. This rate is about 10–100 times higher than the theoretical mass accretion rate of low-mass protostars (10^{-6}–$10^{-5}\ M_\odot\ {\rm yr}^{-1}$: Larson 2003). According to the numerical simulations of the protostellar evolution including episodic accretion (Vorobyov & Basu 2006; Machida et al. 2011), the mass accretion rate in the earliest evolutionary stage up to 10^4 yr rapidly oscillates between $10^{-6}\ M_\odot\ {\rm yr}^{-1}$ and $10^{-4}\ M_\odot\ {\rm yr}^{-1}$, where its average rate gradually decreases with evolution. Although the mass accretion rate obtained for CMM3A overlaps the high end of the above range, it is still higher than the average accretion rate. Note that the dynamical timescale of the outflow might be underestimated, because the SMA observation may miss the older extended outflow components. Nevertheless, the high accretion rate is robust, even if the dynamical timescale were 10^4 yr.

The bolometric luminosity can be estimated from the mass accretion rate as:

$$L_{\rm bol} = \frac{GM_{\rm star}\dot{M}_{\rm acc}}{r_{\rm star}} \qquad (3)$$

where $L_{\rm bol}$ is the bolometric luminosity, $M_{\rm star}$ and $r_{\rm star}$ are the mass and radius of the protostar, respectively, and $\dot{M}_{\rm acc}$ is the mass accretion rate. Using the protostellar mass of CMM3A (0.1–0.5 $M_\odot$) and the accretion rate ($5 \times 10^{-5} - 4 \times 10^{-3}\ M_\odot\ {\rm yr}^{-1}$), the average bolometric luminosity is estimated to be as high as $63 \sim 25{,}000\ L_\odot$. Here, we employ the conventional protostellar radius of 2.5 $R_\odot$ (e.g., Palla 1999; Baraffe & Chabrier 2010). This is likely higher than the current

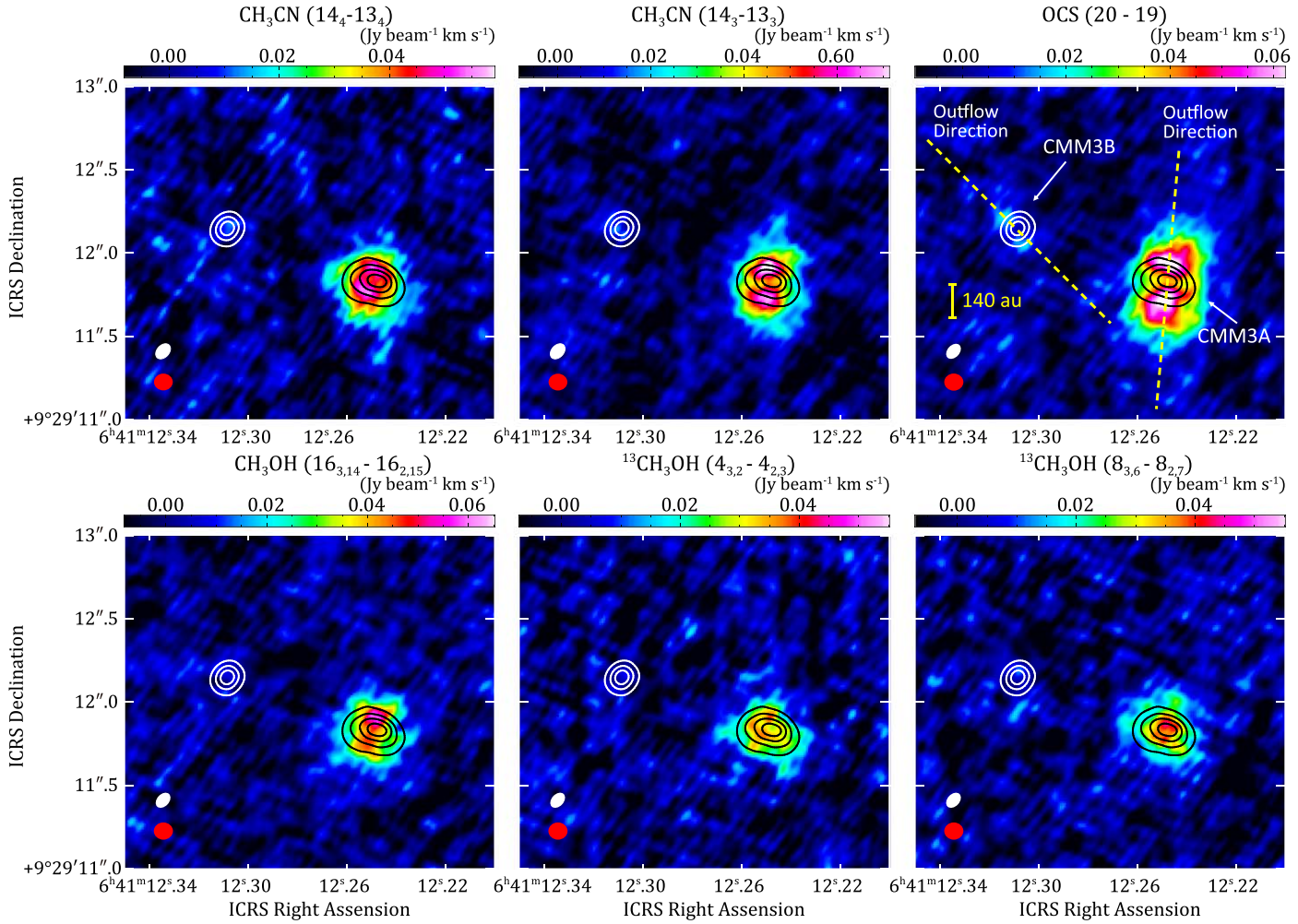

Figure 7. The zeroth moment maps of the emission lines listed in Table 1. The velocity range of integration is from 2.5 to 12.5 km s^{-1}. The rms noises are 4.9×10^{-3} Jy beam^{-1}km s^{-1} for OCS (20 − 19), 5.5×10^{-3} Jy beam^{-1}km s^{-1} for CH_3OH ($16_{3,14} - 16_{2,15}$), $^{13}CH_3OH$ ($4_{3,2} - 4_{2,3}$), and $^{13}CH_3OH$ ($8_{3,6} - 8_{2,7}$), and 6.0×10^{-3} Jy beam^{-1}km s^{-1} for CH_3CN ($14_4 - 13_4$) and CH_3CN ($14_3 - 13_3$). The continuum emission at 1.3 mm is displayed in contours with steps of 50σ where σ is 0.13 mJy beam^{-1}. The white ellipse represent the beam size of the 1.3 mm continuum image. The red ellipse represents the beam size of each zeroth moment map. The yellow dashed lines indicate outflow directions which are −5° and 50° in P.A., for CMM3A and CMM3B, respectively, based on the results reported by Watanabe et al. (2017).

bolometric luminosity of $50 \pm 10\,L_\odot$ reported by Maury et al. (2009), although the lower end of the estimated range is close to the observed luminosity. It should be noted that the observed luminosity is not the luminosity of a single protostar, but the total luminosity of the CMM3 region. The luminosity estimated from the accretion rate is regarded as the value over the time from the protostellar birth, which can be different from the current one. Nevertheless, the difference is large.

This discrepancy on the mass accretion rate could be mitigated in the case of a high accretion rate. Hosokawa & Omukai (2009) pointed out that the protostellar radius can be as high as 100 $R_\odot$ for the accretion rate of $10^{-3}\,M_\odot$ yr^{-1}. A larger protostellar radius for a larger accretion rate is also theoretically predicted (Stahler et al. 1986). Although the evolution of the protostellar radius is complicated (e.g., Kuiper & Hosokawa 2018), the above conventional assumption of the protostellar radius of 2.5 $R_\odot$ is likely underestimated for CMM3A. If it were 100 $R_\odot$, the luminosity is roughly estimated to be 2–630 $L_\odot$.

The origin of the high accretion rate of CMM3A is not definitively clear but may be related to the binary formation in the environment of NGC2264 cluster. In this relation, the accretion rate for CMM3B is of particular interest. Moreover, we have revealed that the disk/envelope structure is significantly different between CMM3A and CMM3B: the latter harbors more compact disk and more extended envelope than the former. This difference also seems to be related to the mechanism of the binary formation. Thus, we need the protostellar mass and the accretion rate of CMM3B for further investigations on the origin and the fate of this binary system. For this purpose, centimeter wave line observations, where the dust opacity is significantly lower than the present study case, are essential, as revealed for NGC1333 IRAS4A by De Simone et al. (2020). Since NGC2264 CMM3 is relatively close to the Sun and its structure can readily be investigated in detail, it may provide us with important information on the early stage of intermediate-mass protobinary systems.

3.5. A Hint of Rotation of the Outflow

The zeroth moment map of OCS (Figure 7) shows that the emission around CMM3A extends along the outflow direction over the disk region traced by the continuum image. The first

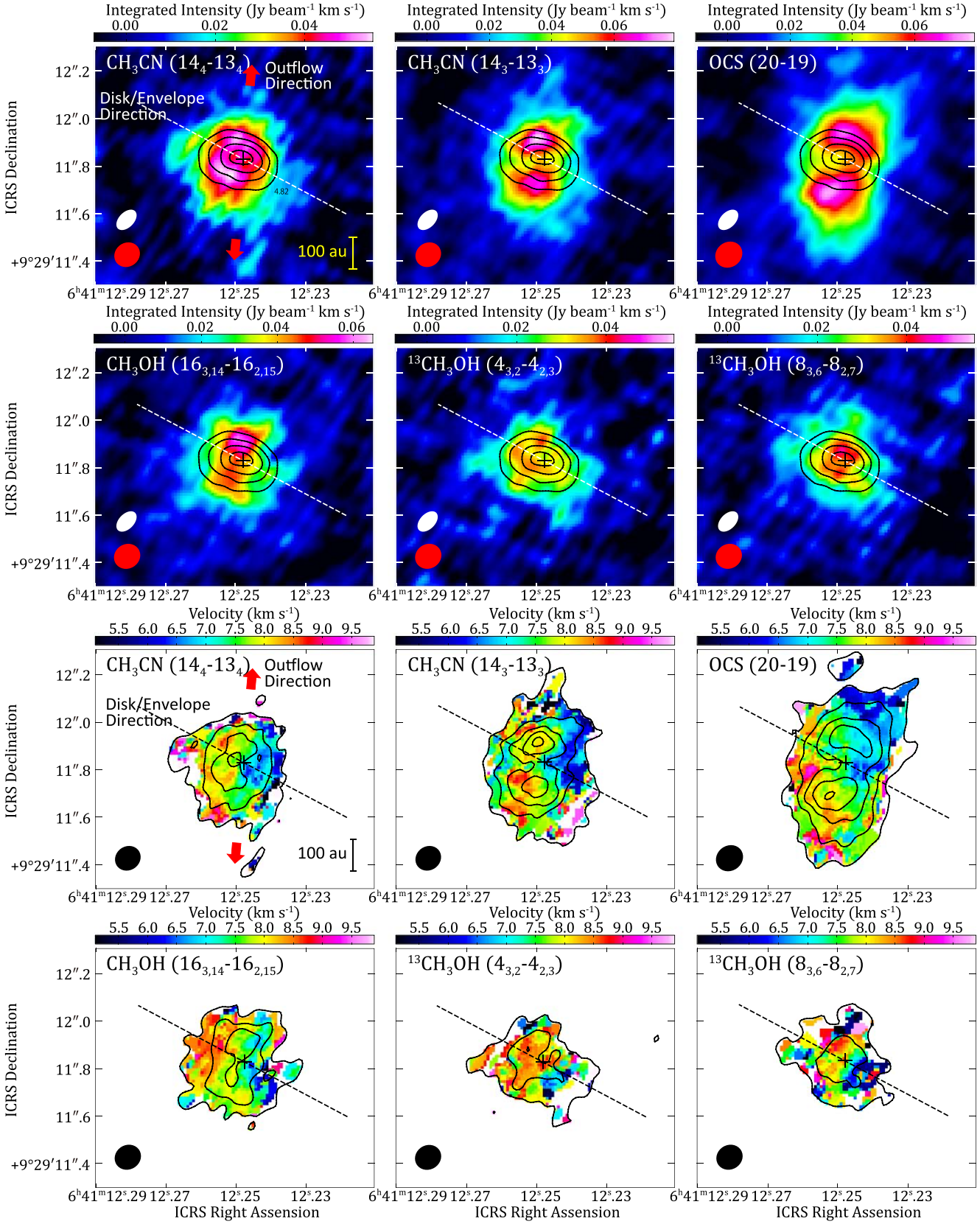

Figure 8. The zeroth and first moment maps of the emission lines listed in Table 1 at CMM3A. The velocity range of integration is from 2.5 to 12.5 km s^{-1}. The black ellipse represents the beam size. The black crosses represents the protostellar position of CMM3A. The continuum emission at 1.3 mm is displayed on the zeroth moment maps by contours with steps of 50σ where σ is 0.13 mJy beam^{-1}. The contours on the first moment maps are 3, 6, 9, and 12σ of the zeroth moment map of each emission line. The region where the zeroth moment is lower than 3σ is clipped in the first moment maps. The red arrows indicates outflow directions of CMM3A ($-5°$ in P.A.; see caption of Figure 7). The disk/envelope direction is estimated from the 1.3 mm continuum images (P.A. = 62°).

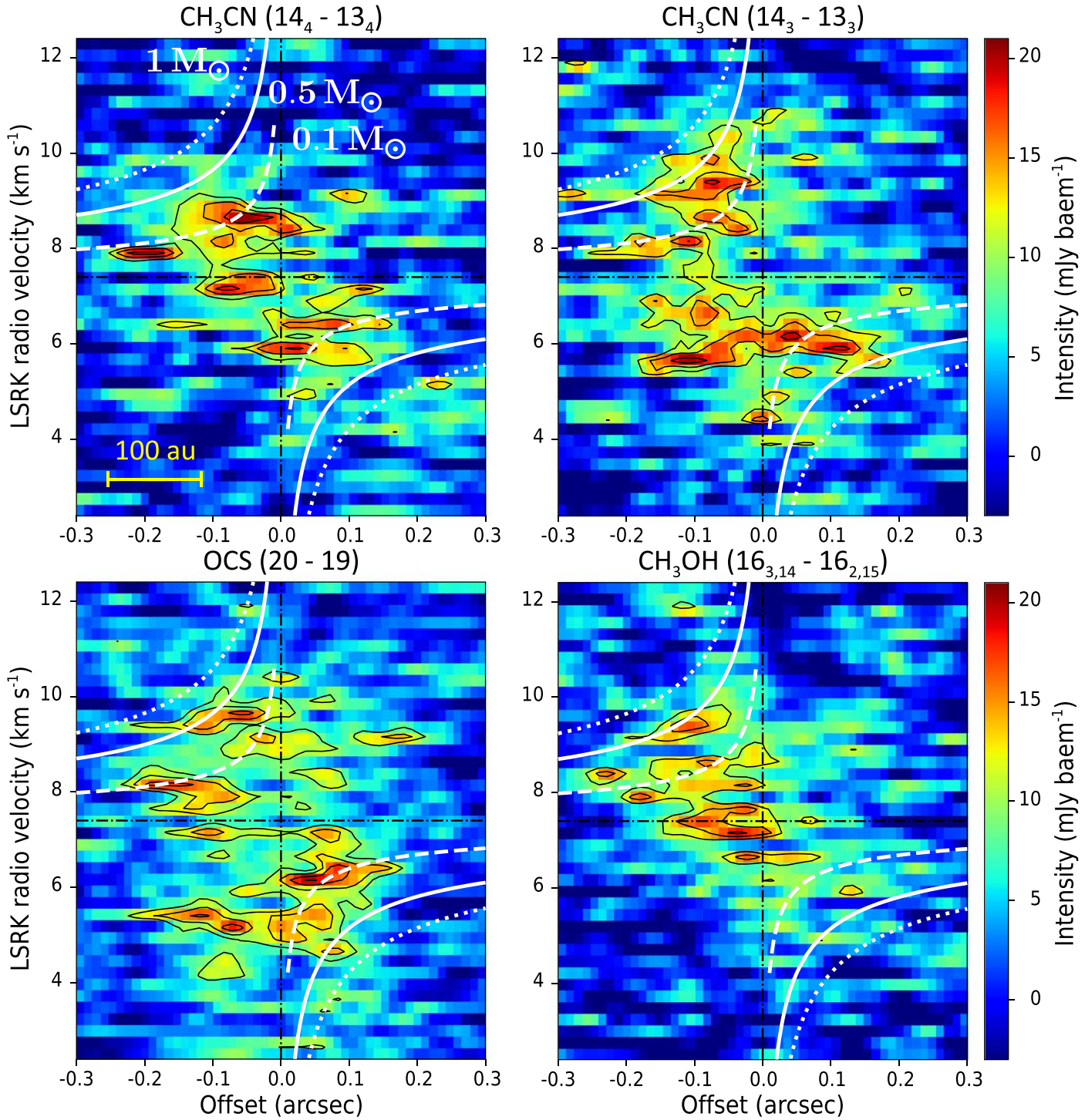

Figure 9. The PV diagrams of CH_3CN, OCS, and CH_3OH. The contours are 3, 4, and 5σ, where 1σ is 3×10^{-3} Jy beam^{-1}. The PV diagrams are made along the disk/envelope direction estimated from the 1.3 mm and 2.0 mm continuum images (P.A. = 62°). The horizontal axis is the distance from the 1.3 mm continuum peak, and the vertical axis is the velocity along the line of the sight. The horizontal line represents the systemic velocity of CMM3A (7.4 km s^{-1}: Watanabe et al. 2017). Dashed, solid, and dotted curves represent the Keplerian rotation with the protostellar mass of 0.1 $M_\odot$, 0.5 $M_\odot$, and 1 $M_\odot$, respectively. The inclination angle is assumed to be 65°.

moment map of OCS (Figure 8) shows the velocity gradient in the outflow direction. The blueshifted velocity is dominant in the northwestern part, while the redshifted velocity is dominant in the southeastern part. Thus, the OCS line likely traces the foot region of the outflow of CMM3A in addition to the disk/envelope system. In Figure 8, a velocity gradient across the outflow lobes is marginally visible. Figure 10 shows the spectral line profiles of OCS toward several positions in the outflow. The velocity difference is clearly seen between the eastern and western edges of the outflow lobes: the eastern edges are slightly redshifted, while the western edges are slightly blueshifted. This also suggests a velocity gradient across the outflow lobes. This velocity gradient can be interpreted most likely as the rotating motion of the outflow,

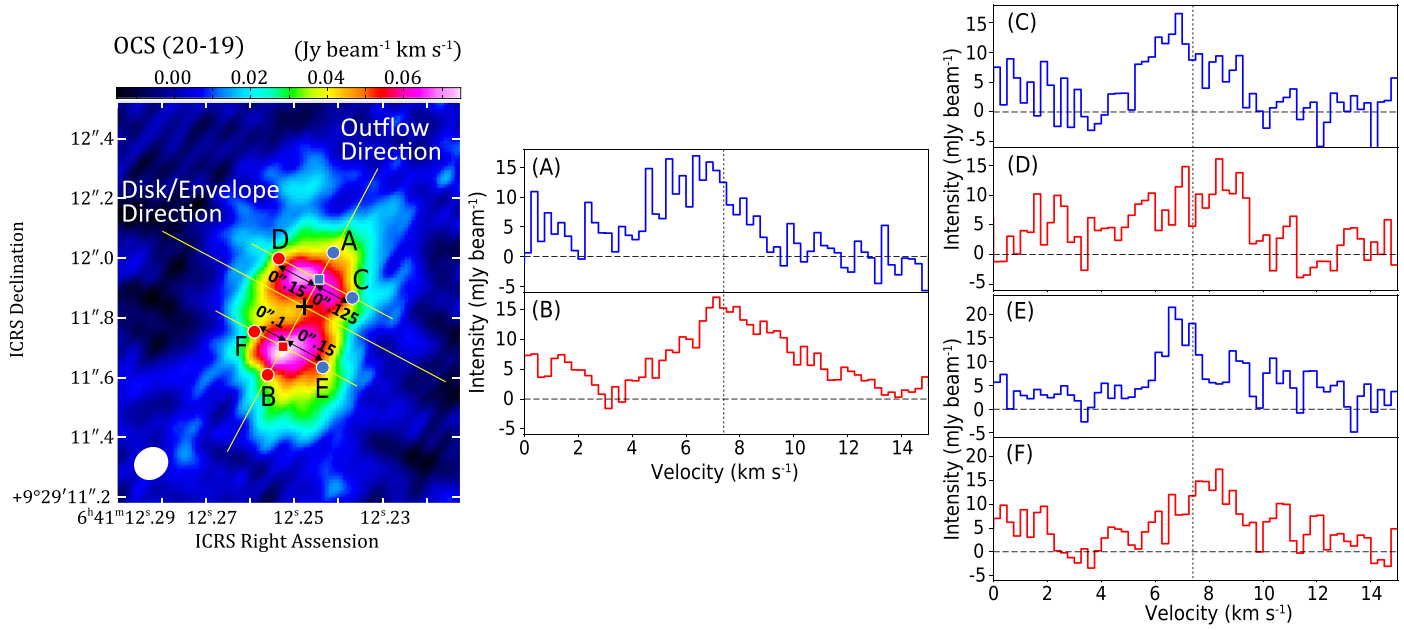

Figure 10. The spectrum of OCS ($J = 20 - 19$) emission. The black cross represents the protostellar position of CMM3A. The white ellipse represents the beam size. The vertical and horizontal lines of each panel represent the systemic velocity of CMM3A (7.4 km s^{-1}: Watanabe et al. 2017) and the ground level (0 Jy beam^{-1}), respectively.

as revealed in other sources (Orion KL Source I: Hirota et al. 2017; L483: Oya et al. 2018 NGC1333; IRAS4C: Zhang et al. 2018). From Figure 10, the rotating velocity of the outflow along the line of sight is ∼1.0 km s^{-1} at the radius of ∼0.″15 (∼100 au). Assuming an inclination angle of 65°, the specific angular momentum of the outflow is estimated to be $\sim 6 \times 10^{-4}$ km s^{-1} pc, which is roughly comparable to the specific angular momentum of the outflow from low-mass protostars (e.g., Oya et al. 2018; Zhang et al. 2018). Here, a caveat is that the velocity gradient across the outflow lobes could reflect the rotating motion of the ambient envelope. Nevertheless, we think that the outflow rotation case is more reasonable, considering the morphology of the OCS emission extending along the outflow direction. The zeroth moment map of the OCS emission also shows a faint emission in CMM3B, which is distributed along the outflow direction of CMM3B (in the northeast–southwest direction; Watanabe et al. 2017). However, the emission line is so faint around CMM3B that the velocity gradient in the disk/envelope direction is not detected in this observation.

For protostars to evolve, the accreting gas needs to lose its angular momentum. The rotation of the outflow is suggested as a possible candidate of the mechanism of angular momentum extraction (e.g., Tomisaka 2002; Anderson et al. 2003; Machida et al. 2008; Oya et al. 2018). To take the angular momentum away, the outflow needs to have more specific angular momentum (angular momentum divided by its mass) than the accreting gas. If the observed velocity gradient across the outflow lobes originates from the outflow rotation, the specific angular momentum of the outflow is estimated above to be $\sim 6 \times 10^{-4}$ km s^{-1} pc, which is comparable to the specific angular momentum of the Keplerian disk at a radius of 35–170 au for the range of the protostellar mass (0.1–0.5 $M_\odot$). This radius would provide us with rough estimate of the launching point of the outflow (Zhang et al. 2018). Such a relatively large launching radius suggests the disk wind caused by magnetocentrifugal effect (e.g., Konigl & Pudritz 2000; Machida et al. 2008; Machida & Hosokawa 2013). However, we apparently need higher quality data for the disk rotation and the outflow rotation for further quantitative analyses.

4. Summary

We conducted high-angular-resolution observations of NGC 2264 CMM3 with ALMA. The principal results of this study are summarized as follows.

1. Continuum images of CMM3A and CMM3B observed at a beam size of 0.″1 × 0.″1 (∼70 au) are decomposed to a compact component and an extended component by double 2D Gaussian fitting. The compact component of CMM3A seems to trace the disk structure. The inclination angle of the disk of CMM3A is estimated to be larger than 65°.
2. The spectral index (α) between 0.8 and 2.0 mm is evaluated from the total flux to be 2.4–2.7 and 2.4–2.6 for CMM3A and CMM3B, respectively. Considering that CMM3A and CMM3B are young protostars (∼1000 yr), the spectral index suggests high dust opacity of CMM3A and CMM3B, although a possibility of the grain growth cannot be ruled out completely. Thus, the very sparse line emission in CMM3B likely originates from the dust opacity effect.
3. The distributions of emission lines of CH_3CN and CH_3OH in CMM3A are found to have an intensity depression in the disk midplane. This can be explained by the high optical depths of the dust emission and the line emission.
4. In the emission lines of CH_3CN, CH_3OH, and $^{13}CH_3OH$, we find the rotation motion of CMM3A. The protostellar mass of CMM3A is roughly evaluated to be about 0.1–0.5 $M_\odot$ by assuming Keplerian rotation. The mass accretion rate of CMM3A is estimated to be $5 \times 10^{-5} - 4 \times 10^{-3}$ $M_\odot$ yr^{-1}. This rate is higher than that of typical low-mass protostars.

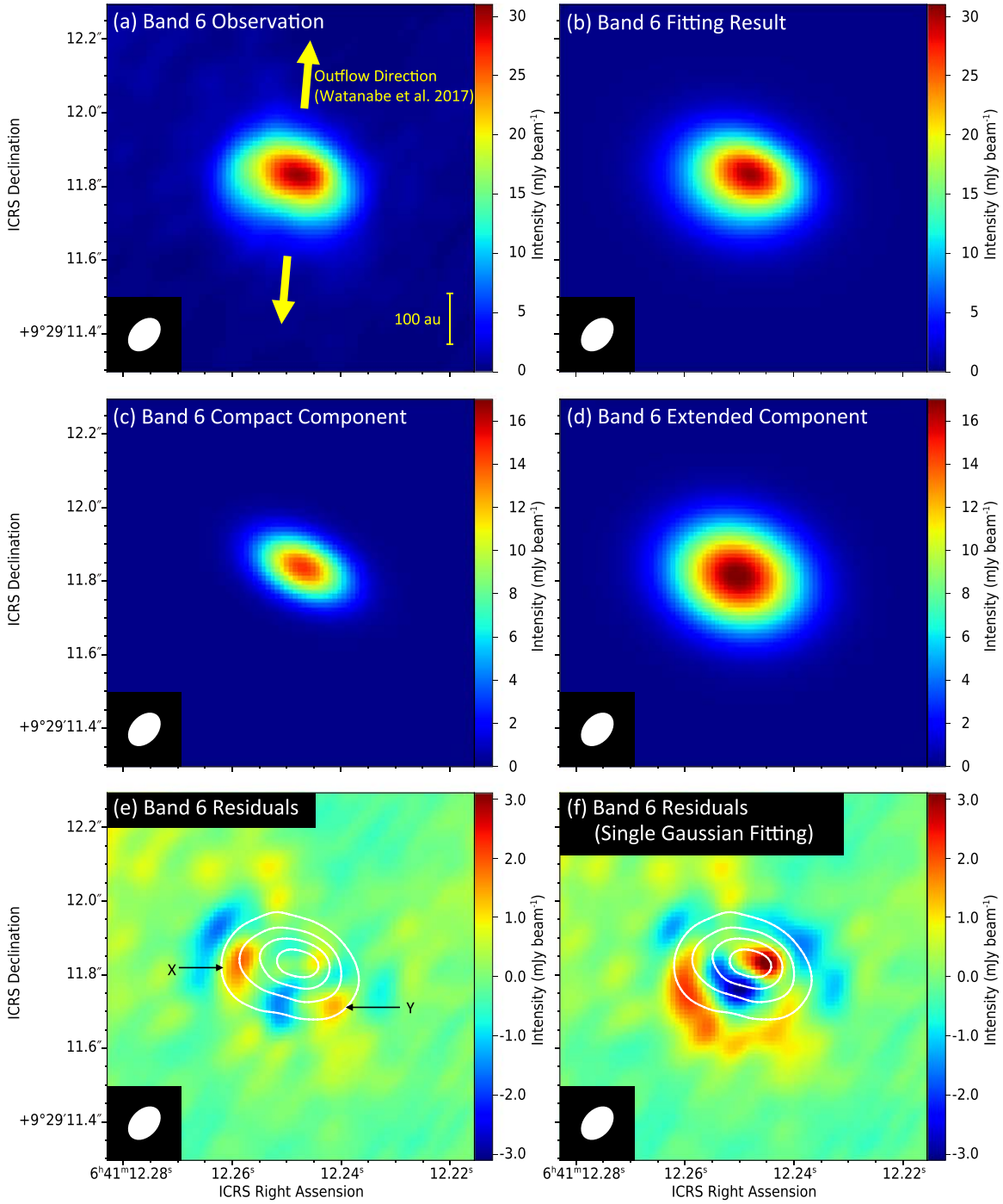

Figure 11. (a) The 1.3 mm (Band 6) continuum image of CMM3A. (b) The result of double 2D Gaussian fit. (c), (d) The compact and extended components of the fitted double 2D Gaussian convolved with the beam. (e) Residuals of the double 2D Gaussian fitting. (f) Residuals of the single 2D Gaussian fitting for comparison. The continuum emission at 1.3 mm is displayed in contours with steps of 50σ where σ is 1.3×10^{-4} Jy beam^{-1} in (e) and (f). X and Y denote the position of the systematic residuals also seen in Figure 2.

5. We find a hint of the rotating motion of the outflow of CMM3A in the OCS line. Since the specific angular momentum of the outflow is comparable to the disk, this rotating outflow can contribute to the extraction of the angular momentum from the accreting gas.

This study used the ALMA data set ADS/JAO. ALMA#2018.1.01647.S. ALMA is a partnership of the European Southern Observatory, the National Science Foundation (USA), the National Institutes of Natural Science (Japan), the National Research Council (Canada), and the NSC and ASIAA (Taiwan), in cooperation with Republic of Chile. The Joint ALMA Observatory is operated by ESO, the AUI/NRAO, and NAOJ. The authors acknowledge the ALMA staff for their excellent support. This study is supported by Grant-in-Aids from Ministry of Education, Culture, Sports, Science, and Technologies of Japan (18H05222, 19H05069, and 19K14753).

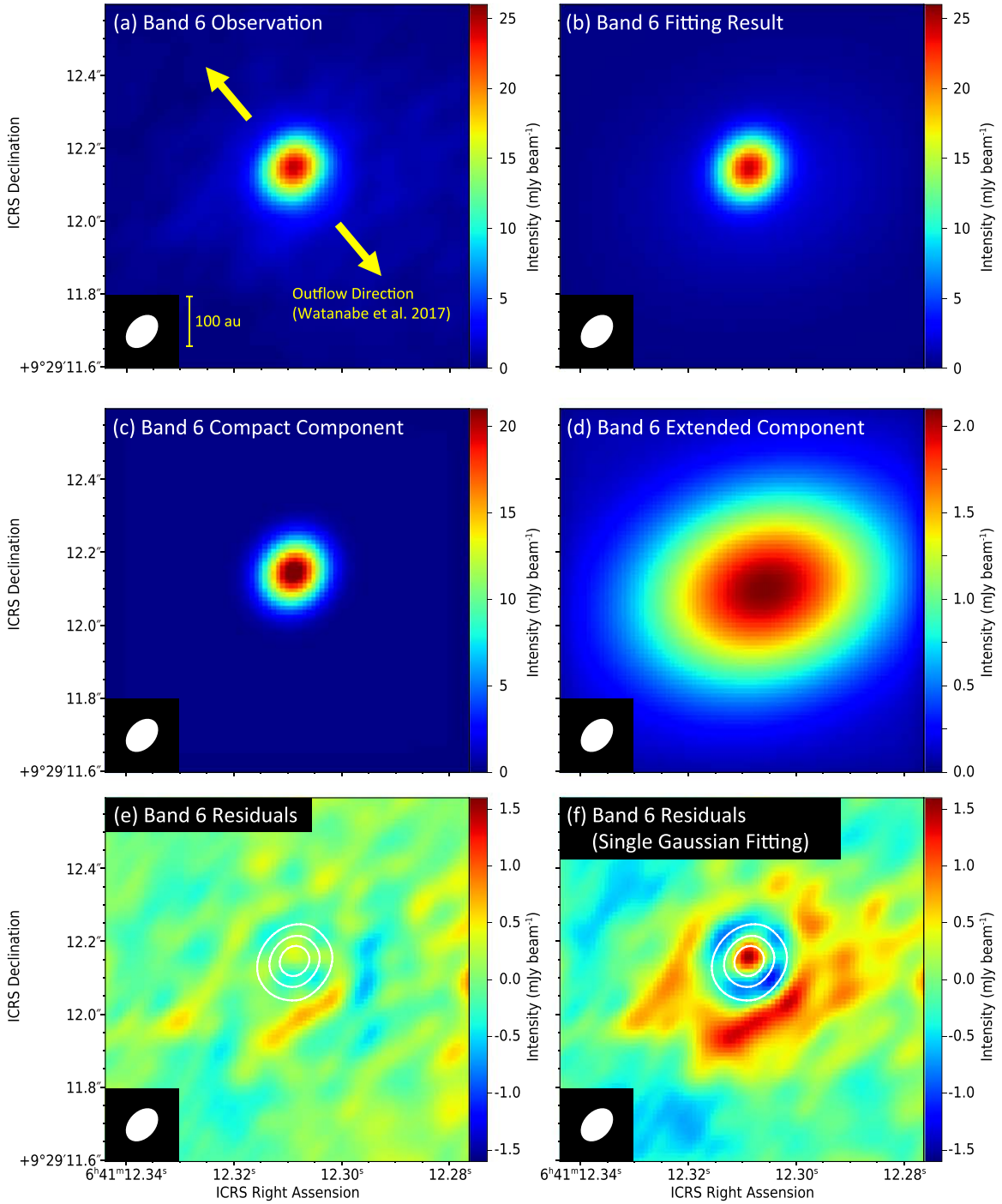

Figure 12. (a) The 1.3 mm (Band 6) continuum image of CMM3B. (b) The result of the double 2D Gaussian fitting. (c), (d) The compact and extended components of the fitted double 2D Gaussian convolved with the beam. Note that the color scale is different between (c) and (d). (e) Residuals of the double 2D Gaussian fitting. (f) Residuals of the single 2D Gaussian fitting for comparison. The continuum emission at 1.3 mm is displayed in contours with steps of 50σ where σ is 1.3×10^{-4} Jy beam^{-1} in (e) and (f).

Appendix
Results of the 2D Gaussian Fit in the 1.3 mm Band

We present the results of 2D Gaussian fit toward CMM3A (Figure 11) and CMM3B (Figure 12) in the 1.3 mm band. The single 2D Gaussian fit for CMM3A and CMM3B reveals residuals similar to the corresponding case for the 2.0 mm data (Section 3.2), as shown in Figures 11(f) and 12(f), respectively. Then, we conduct the double 2D Gaussian fit as in the case of the 2.0 mm data (Figures 11(a)–(d) and Figures 12(a)–(d) for CMM3A and CMM3B, respectively. The derived parameters are shown in Table 2. The systematic residuals are almost eliminated (Figures 11(e) and 12(e) for CMM3A and CMM3B, respectively).

ORCID iDs

Yoshimasa Watanabe https://orcid.org/0000-0002-9668-3592
Yoko Oya https://orcid.org/0000-0002-0197-8751

Nami Sakai https://orcid.org/0000-0002-3297-4497
Ana López-Sepulcre https://orcid.org/0000-0002-6729-3640
Sheng-Yuan Liu https://orcid.org/0000-0003-4603-7119
Yichen Zhang https://orcid.org/0000-0001-7511-0034
Takeshi Sakai https://orcid.org/0000-0003-4521-7492
Tomoya Hirota https://orcid.org/0000-0003-1659-095X
Satoshi Yamamoto https://orcid.org/0000-0002-9865-0970

References

Allen, D. A. 1972, ApJ, 172, L55
Anderson, J. M., Li, Z.-Y., Krasnopolsky, R., & Blandford, R. D. 2003, ApJL, 590, L107
Baraffe, I., & Chabrier, G. 2010, A&A, 521, A44
Codella, C., Bianchi, E., Tabone, B., et al. 2018, A&A, 617, A10
De Simone, M., Ceccarelli, C., Codella, C., et al. 2020, ApJL, 896, L3
Duchêne, G., & Kraus, A. 2013, ARA&A, 51, 269
Endres, C. P., Schlemmer, S., Schilke, P., Stutzki, J., & Müller, H. S. P. 2016, JMoSp, 327, 95
Friesen, R. K., Pon, A., Bourke, T. L., et al. 2018, ApJ, 869, 158
Furuya, R. S., Cesaroni, R., & Shinnaga, H. 2011, A&A, 525, A72
Gerin, M., Pety, J., Commerçon, B., et al. 2017, A&A, 606, A35
Hirota, T., Machida, M. N., Matsushita, Y., et al. 2017, NatAs, 1, 0146
Hosokawa, T., & Omukai, K. 2009, ApJ, 691, 823
Ilee, J. D., Cyganowski, C. J., Brogan, C. L., et al. 2018, ApJL, 869, L24
Konigl, A., & Pudritz, R. E. 2000, in Protostars and Planets IV, ed. V. Mannings et al. (Tucson, AZ: Univ. Arizona Press), 759
Kuiper, R., & Hosokawa, T. 2018, A&A, 616, A101
Lada, C. J., & Lada, E. A. 2003, ARA&A, 41, 57
Larson, R. B. 2003, RPPh, 66, 1651
Lee, C.-F., Li, Z.-Y., Codella, C., et al. 2018, ApJ, 856, 14
Li, A., & Draine, B. T. 2001, ApJ, 554, 778
Liu, H. B. 2019, ApJL, 877, L22
López-Sepulcre, A., Sakai, N., Neri, R., et al. 2017, A&A, 606, A121
Machida, M. N., & Hosokawa, T. 2013, MNRAS, 431, 1719
Machida, M. N., Inutsuka, S., & Matsumoto, T. 2008, ApJ, 676, 1088
Machida, M. N., Inutsuka, S., & Matsumoto, T. 2011, ApJ, 729, 42
Maíz Apellániz, J. 2019, A&A, 630, A119
Maureira, M. J., Pineda, J. E., Segura-Cox, D. M., et al. 2020, ApJ, 897, 59
Maury, A. J., André, P., & Li, Z.-Y. 2009, A&A, 499, 175
Maury, A. J., André, P., Testi, L., et al. 2019, A&A, 621, A76
Ossenkopf, V., & Henning, T. 1994, A&A, 291, 943
Oya, Y., Sakai, N., López-Sepulcre, A., et al. 2016, ApJ, 824, 88
Oya, Y., Sakai, N., Watanabe, Y., et al. 2018, ApJ, 863, 72
Oya, Y., & Yamamoto, S. 2020, ApJ, 904, 185
Palla, F. 1999, in NATO Advanced Study Institute (ASI) Series C, Vol. 540, The Origin of Stars and Planetary Systems, ed. C. J. Lada & N. D. Kylafis (Dordrecht: Kluwer), 375
Peretto, N., André, P., & Belloche, A. 2006, A&A, 445, 979
Pérez, L. M., Chandler, C. J., Isella, A., et al. 2015, ApJ, 813, 41
Pickett, H. M., Poynter, R. L., Cohen, E. A., et al. 1998, JQSRT, 60, 883
Raghavan, D., McAlister, H. A., Henry, T. J., et al. 2010, ApJS, 190, 1
Sahu, D., Liu, S.-Y., Su, Y.-N., et al. 2019, ApJ, 872, 196
Saruwatari, O., Sakai, N., Liu, S.-Y., et al. 2011, ApJ, 729, 147
Stahler, S. W., Palla, F., & Salpeter, E. E. 1986, ApJ, 302, 590
Takakuwa, S., Saigo, K., Matsumoto, T., et al. 2020, ApJ, 898, 10
Thompson, R. I., Corbin, M. R., Young, E., & Schneider, G. 1998, ApJ, 492, L177
Tobin, J. J., Bourke, T. L., Mader, S., et al. 2019, ApJ, 870, 81
Tobin, J. J., Looney, L. W., Li, Z.-Y., et al. 2016, ApJ, 818, 73
Tobin, J. J., Looney, L. W., Li, Z.-Y., et al. 2018, ApJ, 867, 43
Tobin, J. J., Sheehan, P. D., Megeath, S. T., et al. 2020, ApJ, 890, 130
Tomisaka, K. 2002, ApJ, 575, 306
Vorobyov, E. I., & Basu, S. 2006, ApJ, 650, 956
Ward-Thompson, D., Zylka, R., Mezger, P. G., & Sievers, A. W. 2000, A&A, 355, 1122
Watanabe, Y., Chiba, Y., Sakai, T., et al. 2021, PASJ, 73, 372
Watanabe, Y., Sakai, N., López-Sepulcre, A., et al. 2017, ApJ, 847, 108
Zhang, Y., Higuchi, A. E., Sakai, N., et al. 2018, ApJ, 864, 76